

Quantum-statistical theory for laser-tuned transport and optical conductivities of dressed electrons in $\alpha - \mathcal{T}_3$ materials

Andrii Iurov^{1,2*}, Liubov Zhemchuzhna³, Dipendra Dahal³, Godfrey Gumbs^{3,4}, and Danhong Huang^{5,2}

¹*Department of Physics and Computer Science, Medgar Evers College of City University of New York, Brooklyn, NY 11225, USA*

²*Center for High Technology Materials, University of New Mexico, 1313 Goddard SE, Albuquerque, New Mexico, 87106, USA*

³*Department of Physics and Astronomy, Hunter College of the City University of New York, 695 Park Avenue, New York, New York 10065, USA*

⁴*Donostia International Physics Center (DIPC), P de Manuel Lardizabal, 4, 20018 San Sebastian, Basque Country, Spain*

⁵*Air Force Research Laboratory, Space Vehicles Directorate, Kirtland Air Force Base, New Mexico 87117, USA*

(Dated: August 21, 2019)

In the presence of external off-resonance and circularly-polarized irradiation, we have derived a many-body formalism and performed a detailed numerical analysis for both the conduction and optical currents in $\alpha - \mathcal{T}_3$ lattices. The calculated complex many-body dielectric function, as well as conductivities of displacement and transport currents, display strong dependence on the lattice-structure parameter α , especially approaching the graphene limit with $\alpha \rightarrow 0$. Unique features in dispersion and damping of plasmon modes are observed with different α values, which are further accompanied by a reduced transport conductivity under irradiation. The discovery in this paper can be used for designing novel multi-functional nanoelectronic and nanoplasmonic devices.

I. INTRODUCTION

So far, the $\alpha - \mathcal{T}_3$ model seems to present prospective opportunities for revolutionizing low-dimensional physics through novel two-dimensional (2D) materials.¹ Its atomic configuration consists of a graphene-type honeycomb lattice along with an additional site, i.e., a hub atom at the center of each hexagon.² An essential structure parameter $\alpha = \tan \phi$, which enters into the low-energy Dirac-Weyl pseudospin-1 Hamiltonian for $\alpha - \mathcal{T}_3$ model, is found to be the ratio between the rim-to-hub and rim-to-rim hopping coefficients. This parameter affects all fundamental electronic properties of the $\alpha - \mathcal{T}_3$ lattice through topological characteristics embedded in its pseudospin-1 wave functions. Parameter α can vary from 0 to 1, corresponding to different types of $\alpha - \mathcal{T}_3$ materials, and the control of it could lead to some important technological applications for electronic and optoelectronic devices. Here, the case with $\alpha = 0$ relates to graphene with a completely separated flat band, whereas $\alpha = 1$ results in a pseudospin-1 dice lattice which has been fabricated and studied considerably.^{3,4} Consequently, the $\alpha - \mathcal{T}_3$ model may be viewed as an interpolation between graphene and the dice lattice (or pseudospin-1 \mathcal{T}_3 model). Its low-energy dispersion consists of a Dirac cone, similar to that for graphene,⁵ as well as a flat band with zero-energy separating the valence from the conduction band for these pseudospin-1 materials.^{6,7}

In recent years, there have been numerous attempts for experimental realization of the $\alpha - \mathcal{T}_3$ model. Its topological characteristics, i.e., a Dirac cone with three bands touching at a single point, was observed in the triplon band structure of $\text{SrCu}_2(\text{BO}_3)_2$, as an example of general Mott-Hubbard insulators.⁸ Moreover, dielectric photonic crystals with zero refractive index also display Dirac cone dispersion at the center of the Brillouin zone under an accidental degeneracy.^{9,10} Most importantly, there exist various types of photonic Lieb lattices,^{11,12} consisting of a 2D array of optical waveguides. Such waveguide-lattice structure is shown to have a three-band structure, including a perfectly flat middle band.

Further to a relatively recent proposal on $\alpha - \mathcal{T}_3$ model, there have been a lot of crucial publications devoted to investigating their magnetic,^{1,13-15} optical,^{16,17} many-body⁷ and electron transport properties,¹⁸⁻²¹ as well as to generalized versions of this model²². A number of compelling properties of graphene and other low-dimensional materials²³ have been realized in $\alpha - \mathcal{T}_3$ materials, including Klein tunneling^{24,25} and Hofstadter butterfly²⁶. Meanwhile, all pseudospin-1 structures also display some previously unknown phenomena resulting from the existence of a flat band in their energy dispersions²⁷, e.g., distinctive plasmon modes with a branch “*pinching*” feature at the Fermi level.⁷

* E-mail contact: aiurov@unm.edu, theorist.physics@gmail.com

We note that an exciting emergent technical application for condensed-matter quantum optics is *Floquet engineering*. This subject leads to a wide-range optical-tuning capability and control of electron optical and transport currents in 2D materials by introducing an off-resonant periodic dressing field in either terahertz or microwave frequency.^{28–34} Such external irradiation imposed on a 2D material produces a dramatic change in most of its electronic properties due to creating so-called *dressed states*. This gives rise to a single quantum entity, consisting of an electron interacting with a photon. It is described by unique energy-dispersion relations, depending on the intensity and polarization of incoming radiation.

Our investigation of these electron dressed states is based on Floquet theory for quantum systems, driven by external periodic potentials. This results in a $\sim 1/(\hbar\omega)$ series expansion, as employed by Floquet-Magnus, Brillouin-Wigner and others,³⁵ and provides an effective analytical tool for investigating light-electron interaction in a variety of novel 2D materials^{36–39} and optically-induced topological surface states⁴⁰ as well.

The modifications of single-particle band structure and wave function greatly affect the many-body dielectric function^{23,41,42} in addition to electron conduction current^{43,44} and conductivity⁴⁵. These changes mainly come from opening an energy gap³⁶ between the valence and conduction bands, as well as from topologically-modified wave functions.⁴⁶ For a linearly-polarized optical dressing field, we find strong in-plane anisotropy, and even the anisotropic dispersion of phosphorene still experiences a lot of changes under this dressing field.⁴⁷

Once Floquet engineering has been applied to $\alpha - \mathcal{T}_3$ materials, we expect some fundamental changes will occur, such as, band-dispersion anisotropy, opening inequivalent energy gaps within each band, breaking down the electron-hole symmetry and valley degeneracy,¹⁶ and topological variation of electron wave functions including their symmetries and the Berry phases.⁴⁸ Interestingly, circularly-polarized radiation can induce a topological phase transition from a gapless semimetal to a topological insulator with a nonzero Chern number.¹⁷ This result acquires a resemblance to a topological insulator, obtained from a periodic array of quantum rings under a circularly-polarized optical field.⁴⁹

The rest of this paper is organized as follows. In Sec. II, electron dressed states by an strong laser field in $\alpha - \mathcal{T}_3$ materials are derived. In Sec. III, the effects of optically-dressed states on many-body dielectric function, plasmon mode and electron optical current are presented. The dressed-state effects on rate for elastic impurity scattering and conduction current are displayed in Sec. IV. Finally, a summary and some remarks are given in Sec. V.

II. VALLEY-SPIN DEPENDENT DRESSED STATES

The optical current of electrons in $\alpha - \mathcal{T}_3$ materials should be driven by a laser field. In the presence of the laser field, bare electron states are obtained by substituting the electron wavevector $\mathbf{k} = \{k_x, k_y\}$ in the Hamiltonian of considered materials with $\mathbf{k} - (e/\hbar) \mathbf{A}(t)$. Here, $\mathbf{A}(t) = (\mathcal{E}_0/\omega) \{\cos(\omega t), \sin(\omega t)\}$ is a spatially-uniform vector potential associated with the applied circularly-polarized light, where \mathcal{E}_0 is the amplitude of the electric-field component of imposed radiation and ω is its angular frequency in the off-resonance regime. As a result, the Hamiltonian will acquire an additional time-dependent term due to light-electron interaction.

In this paper, we employ the Floquet-Magnus perturbation-expansion theory for our calculations. This procedure is applicable to any periodically-driven quantum structure³⁵ so as to obtain valley-degenerate, isotropic and symmetric energy bands near the flat band,⁴⁸ yielding $\varepsilon_0(k, \lambda_0) = 0$ and

$$\varepsilon_\gamma(k, \lambda_0) = \gamma \sqrt{(\lambda_0 c_0/2)^2 + [\hbar v_F k (1 - \lambda_0^2/4)]^2}, \quad (1)$$

where $\gamma = \pm$ for electrons (+) and holes (-), $c_0 = e\mathcal{E}_0 v_F/\omega$ represents the interaction coefficient (energy), v_F is the Fermi velocity, and $\lambda_0 = c_0/(\hbar\omega) = e\mathcal{E}_0 v_F/(\hbar\omega^2)$ is a dimensionless light-electron coupling parameter. We limit our consideration to off-resonance frequencies of the laser field, where the photon energy $\hbar\omega$ greatly exceeds any electron energies, e.g., Fermi energy $E_F = \hbar v_F k_F$ with the Fermi wavenumber $k_F = \sqrt{\pi\rho_0}$ and areal doping density ρ_0 . Consequently, we have $\lambda_0 \ll 1$ in spite of the light intensity $\mathbb{I}_0 = \epsilon_0 c \mathcal{E}_0^2/2 \sim 10 \text{ W/cm}^2$.

The obtained dispersions in Eq. (1) reveal an energy bandgap $E_G = \lambda_0 c_0 \equiv 2\Delta_0$ which is only half of the graphene gap energy with the same interaction coefficient c_0 .³⁶ The electronic states for an irradiated dice lattice, pertaining to the valence and conduction bands, are given by

$$\Psi_\gamma^\tau(\mathbf{k}, \lambda_0) = \frac{1}{\sqrt{\mathcal{N}_\gamma^\tau}} \begin{bmatrix} \tau C_{1,\gamma}^\tau e^{-i\tau\theta_\mathbf{k}} \\ C_{2,\gamma}^\tau \\ \tau (\hbar v_F k)^2 e^{+i\tau\theta_\mathbf{k}} \end{bmatrix}, \quad (2)$$

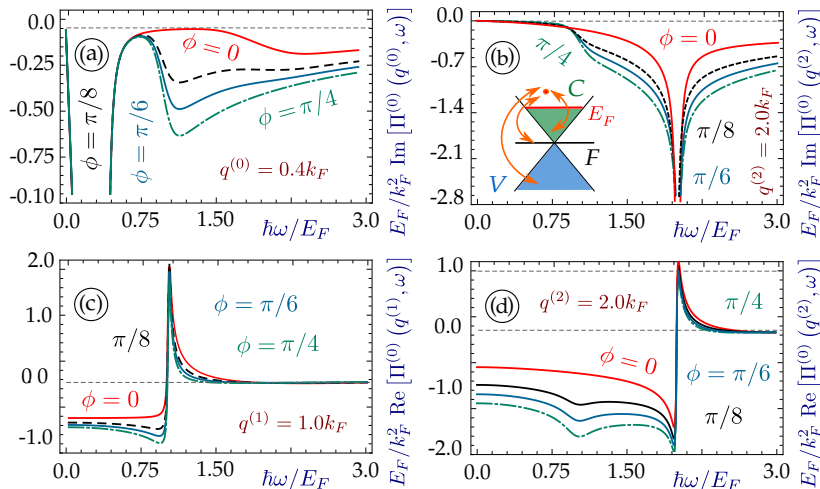


FIG. 1: (Color online) Frequency (ω) and wavevector (q) dependent polarization function $\Pi_0(q, \omega | \phi)$ (in units of k_F^2/E_F) for non-irradiated $\alpha - \mathcal{T}_3$ model ($\lambda_0 = 0$) as a function of $\hbar\omega$ with various phase values ϕ . Here, each panel corresponds to a chosen wavevector $q = q_i$ and each curve is for a specific phase ϕ , as labeled. Two upper panels [(a), (b)] present the imaginary part of $\Pi_0(q, \omega | \phi)$, whereas the two lower ones [(c), (d)] are its real part. The inset in plot (b) illustrates all possible single-particle transitions (red double-arrow curves) contributing to $\Pi_0(q, \omega | \phi)$ at $T = 0$ K with a horizontal red line for the Fermi energy E_F .

where

$$\begin{aligned} \mathcal{C}_{1,\gamma}^\tau(k, \lambda_0) &= (\hbar v_F k)^2 + 2 \left(\delta_\lambda^2 - \gamma \tau \delta_\lambda \sqrt{(\hbar v_F k)^2 + \delta_\lambda^2} \right), \\ \mathcal{C}_{2,\gamma}^\tau(k, \lambda_0) &= \sqrt{2} \gamma (\hbar v_F k) \left(\sqrt{(\hbar v_F k)^2 + \delta_\lambda^2} - \gamma \tau \delta_\lambda \right), \\ \mathcal{N}_\gamma^\tau(k, \lambda_0 \ll 1) &\simeq 4 (\hbar v_F k)^4 - 4 \gamma \tau c_0 \lambda_0 (\hbar v_F k)^3 + 3 [c_0 \lambda_0 (\hbar v_F k)]^2 + \dots \end{aligned} \quad (3)$$

Here, the parameter $\delta_\lambda = 2\lambda_0 c_0 / (4 - \lambda_0^2)$ is different from the actual energy gap $E_G = \lambda_0 c_0 = 2\Delta_0$. For the flat band with $\gamma = 0$, on the other hand, three components of its wave function are not the same and the middle one is nonzero, as expected for a finite energy gap (see Appendix A).

The above electron dressed states share a similarity with an irradiated dice material but are not equivalent to those from a gapped Hamiltonian with an added $\Delta_0 \hat{\Sigma}_z^{(3)}$ term, where $\hat{\Sigma}_z^{(3)}$ represents a (3×3) z -Pauli matrix with the main diagonal $\{1, 0, -1\}$ and is used to describe the effect of a point defect.²⁷

III. PLASMON MODE AND OPTICAL CURRENT

The self-sustaining charge-density longitudinal oscillations, i.e., plasmons, play an important role in determining the optical-current properties of low-dimensional structures.^{23,46,50–52} These include exotic fullerenes and spherical graphitic particles.^{53–55}

The dispersion relation of plasmon modes in the wavevector-frequency (q, ω)-plane is generally determined from the zero of a dielectric function $\epsilon(q, \omega | \phi, \lambda_0)$. In terms of the dynamical polarization function $\Pi_0(q, \omega | \phi, \lambda_0)$, we can write $\epsilon(q, \omega | \phi, \lambda_0) = 1 - (2\pi\alpha_0/q) \Pi_0(q, \omega | \phi, \lambda_0)$, where $\alpha_0 = e^2 / (4\pi\epsilon_0\epsilon_r)$, ϵ_r is the host-material dielectric constant, and the summation over the valley index τ is performed. In addition, we also require $\Pi_0(q, \omega | \phi, \lambda_0)$ in calculating screening to impurity scattering for electron conduction current. The screened potential for a dilute distribution of impurities embedded in a dice lattice has been discussed⁷ as well as for general $\alpha - \mathcal{T}_3$ materials.⁵⁶ Furthermore, we notice $\Pi_0(q, \omega | \phi, \lambda_0)$ of $\alpha - \mathcal{T}_3$ lattices at $T = 0$ K could substantially differ from that of graphene (red curves for $\phi = 0$), as displayed in Fig. 1. This difference is attributed to additional channels for electron transitions resulting from the middle flat band, as depicted in the inset of Fig. 1(b), especially for $\hbar\omega$ close to the Fermi energy E_F .

The complex $\Pi_0(q, \omega | \phi, \lambda_0 = 0)$ at $T = 0$ K for $0 \leq \alpha \leq 1$ (or $0 \leq \phi \leq \pi/4$) are presented in Figs. 1(a)–1(d). Its imaginary part for $q < k_F$ in Fig. 1(a) shows a noticeable peak at a lower $\hbar\omega$ in comparison with graphene (red curve).

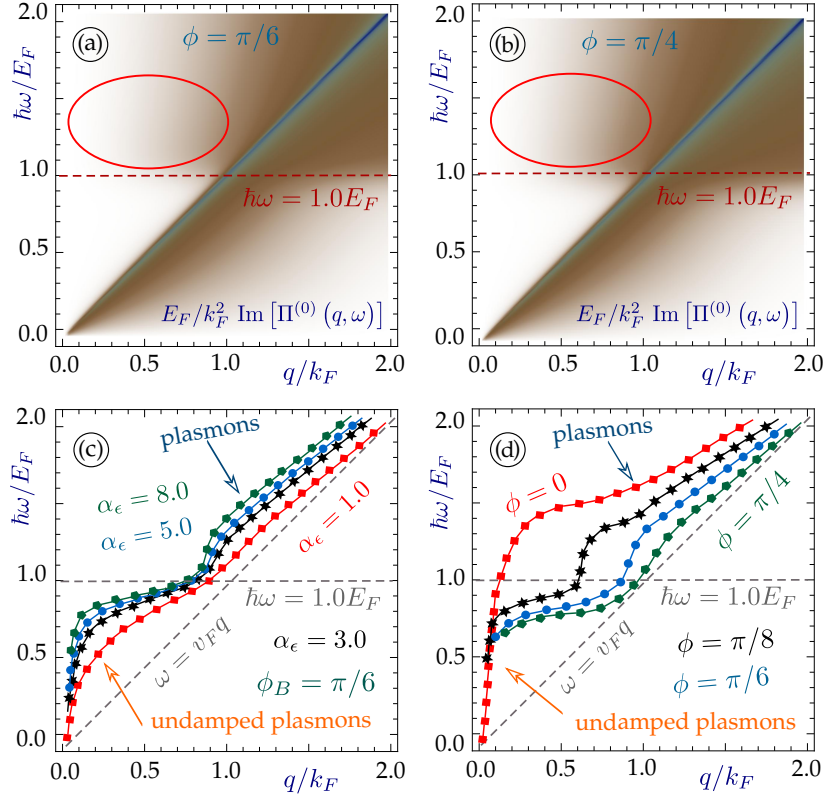


FIG. 2: (Color online) Plasmon damping regions [(a) for $\phi = \pi/6$, (b) for $\phi = \pi/4$] and plasmon branches [(c), (d)] for various types of $\alpha - \mathcal{T}_3$ lattices in the absence of external irradiation ($\lambda_0 = 0$). Two upper panels display $\text{Im}[\Pi_0(q, \omega | \phi)]$, which indicates regions for single-particle excitations. Here, two partially-damping regions above the $\hbar\omega = E_F$ line are highlighted by red circles. Panel (c) presents plasmon dispersions for fixed $\phi = \pi/6$ but different α_0 values, while panel (d) exhibits plasmon modes for fixed $\alpha_0 = 3.0$ and several phase values of ϕ .

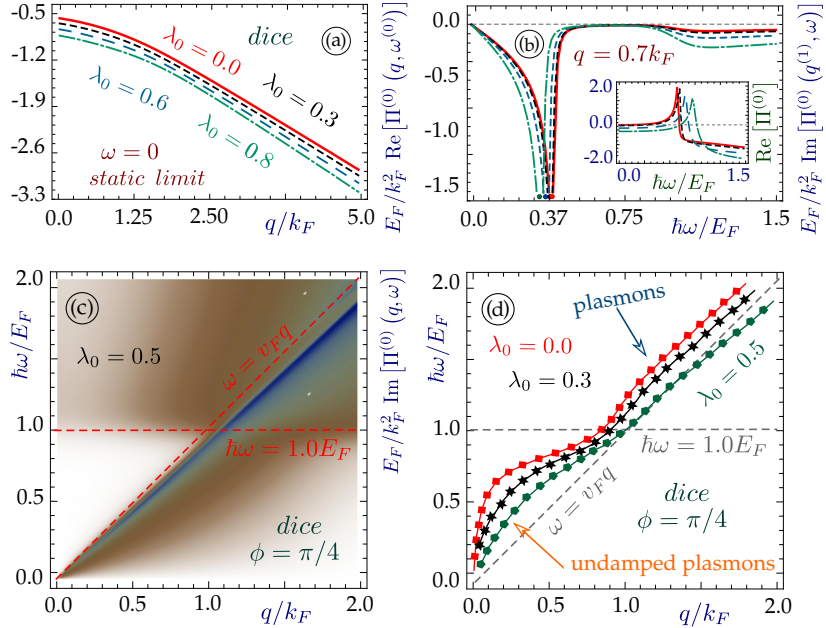


FIG. 3: (Color online) $\Pi_0(q, \omega | \lambda_0)$ in units of k_F^2/E_F [(a)-(c)] and plasmon dispersions (d) for a dice lattice ($\phi = \pi/4$) under a circularly-polarized laser field with various λ_0 values. Panel (a) shows the q dependence of $\text{Re}[\Pi_0(q, \omega = 0 | \lambda_0)]$ in the static limit $\omega = 0$. Plot (b) presents the $\hbar\omega$ dependence of $\text{Im}[\Pi_0(q, \omega | \lambda_0)]$ at $q/k_F = 0.7$, while its inset displays the $\hbar\omega$ dependence for $\text{Re}[\Pi_0(q, \omega | \lambda_0)]$. Plot (c) demonstrates the particle-hole modes $\text{Im}[\Pi_0(q, \omega | \phi, \lambda_0)] \neq 0$ at $\lambda_0 = 0.5$.

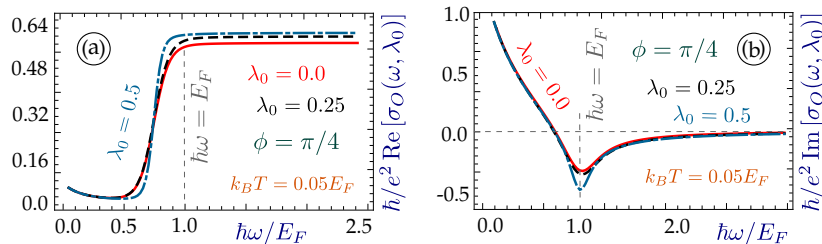


FIG. 4: (Color online) Real (a) and imaginary (b) parts of optical-current conductivity $\sigma_O(\omega | \lambda_0)$ in units of e^2/\hbar for an irradiated dice lattice ($\phi = \pi/4$) as a function of $\hbar\omega$. Here, each curve corresponds to a specific λ_0 value for fixed ϕ and T .

For $q > k_F$ in Fig. 1(b), however, there exists a singular pole scaled as $\sim -1/\sqrt{|v_F^2 q^2 - \omega^2|}$. An accompanied zigzag feature in its real part can also be seen in Figs. 1(c) and 1(d), which reveals the q -dispersion of a plasmon mode.

Physically, the particle-hole continuum comprising the single-particle excitation regions are defined as the regions with $\text{Im}[\Pi_0(q, \omega | \phi, \lambda_0)] \neq 0$. Once a plasmon branch enters into such region, it will suffer from Landau damping resulting in the decay of a plasmon mode into single-particle excitations. Thus, we would concentrate on finding the regions of damping-free plasmon modes with $\text{Im}[\Pi_0(q, \omega | \phi, \lambda_0)] = 0$.

In our calculations, we look for a (q, ω) region in which plasmon modes could be present. In fact, we find that, for all $\alpha - \mathcal{T}_3$ materials, only one *triangle* region appears below the Fermi level E_F plus another one (indicated by a red circle) above the main diagonal ($\omega = v_F q$), as shown in Figs. 2(a) and 2(b). Even though there are additional areas free from Landau damping for $q > 2k_F$, plasmon modes in free-standing 2D materials cannot exist there. Strictly speaking, a plasmon mode will decay once it goes above the line $\hbar\omega/E_F = 1$. Interestingly, the damping strength varies with ϕ and becomes infinitesimally small and even disappears for graphene with $\phi \rightarrow 0$.

The distortion of plasmon dispersions around $\hbar\omega \approx E_F$ in Fig. 2(c) reflects the contributions associated with electron transitions both starting from and ending in the flat band. The influence of this flat band amplifies itself close to the $\hbar\omega/E_F = 1$ line, where various plasmon branches, corresponding to different α_0 values, are expected to be pinched at a single crossing point intersected by the $\hbar\omega/E_F = 1$ line and diagonal to $\hbar\omega = \hbar v_F q$, as found for a dice lattice.⁷ Here, however, we find these distorted plasmon branches with $\phi = \pi/6$ are separated from the diagonal $\hbar\omega = \hbar v_F q$ and only display two peaks below and above the $\hbar\omega/E_F = 1$ line instead of pinching. Moreover, various plasmon branches with different α_0 values will cross the $\hbar\omega/E_F = 1$ line at slightly different q values.

We find one interesting feature by analyzing the degree to which various plasmon modes with a fixed α_0 in Fig. 2(d) are away from the diagonal $\hbar\omega = \hbar v_F q$ for the boundary of single-particle excitations. For $\phi \neq 0$, the plasmon energy is always smaller than that of graphene ($\phi = 0$, red curve). For all finite ϕ , there exist two steps for plasmon energies, which are separated by the $\hbar\omega = E_F$ line, except for $\phi = 0$. The undamped first step under the $\hbar\omega/E_F = 1$ line spans a much larger (up to ten times) q range compared to graphene. For $q \ll E_F/(\hbar v_F)$, all plasmon modes become nearly degenerate, corresponding to the electron transitions across the Fermi energy within the upper Dirac cone. On the other hand, the electron transitions between the flat band and the upper Dirac cone are associated with the range around $q \approx E_F/(\hbar v_F)$ in Fig. 2(d). Furthermore, the electron transitions resulting from two Dirac cones relate to the $q \geq 2E_F/(\hbar v_F)$ range. In summary, we believe the best condition for observing the ϕ -dependence of plasmon dispersions and damping is around $\phi = 0$ because the results for $\phi = \pi/6$ and a dice lattice show only little difference in Fig. 2(d).

Next, we turn our attention to the plasmon dispersions of a dice lattice in the presence of a circularly-polarized laser field. The dice lattice ($\phi = \pi/4$) becomes the most different entity compared to graphene ($\phi = 0$), for the latter the effect of circularly-polarized light is simply adding a band gap (via a $\hat{\Sigma}_z^{(2)}$ term) to the bare Dirac Hamiltonian.^{36,46} The distinctive feature of a dice lattice is that $\text{Re}[\Pi_0(q, \omega = 0 | \lambda_0)]$ no longer becomes a constant within the region of $q < 2k_F$, as demonstrated in Fig. 3(a). Furthermore, as λ_0 increases from zero, the negative peak of $\text{Im}[\Pi_0(q, \omega | \lambda_0)]$ shifts downwards in $\hbar\omega$, while the positive peak of $\text{Re}[\Pi_0(q, \omega | \lambda_0)]$ shifts upwards, as seen in Fig. 3(b) and its inset.

For an irradiated dice lattice, Landau damping is greatly enhanced and shifted downward below the main diagonal $\omega = v_F q$, as found in Fig. 3(c). Although the laser field does not affect the undamped plasmon modes in the triangle region determined by $\omega > v_F q$ and $\hbar\omega/E_F < 1$, their dispersions are significantly modified beyond this triangle region above the diagonal, as presented in Fig. 3(d). Meanwhile, the plasmon energy decreases with increasing λ_0 , similar to the single-electron dispersion in the presence of an energy gap.⁴⁶ However, no similarity to plasmon dispersions of graphene is found due to the addition of a middle flat band. It is worthwhile to mention that the plasmon branch extends into the region below the main diagonal for large λ_0 values.

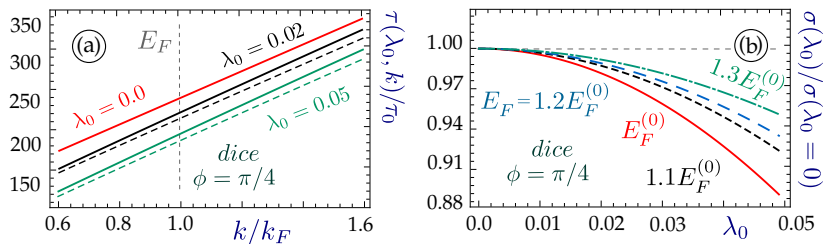


FIG. 5: (Color online) Transport conductivity $\sigma_T(\lambda_0)$ for an irradiated dice lattice. Panel (a) displays the relaxation time $\tau(k, \lambda_0)$ in units of $\tau_0 = 2\hbar E_F^{(0)}/(\pi n_i \alpha_0^2)$ as a function of wavevector k for various electron-light coupling constants λ_0 as labeled, where $E_F^{(0)}$ represents the Fermi energy for the case with $\mathcal{E}_0 = 0$. The dashed curves show the corresponding results without taking into account the laser-induced modification to the static dielectric function. Plot (b) presents the ratio $\sigma_T(\lambda_0)/\sigma_T(\lambda_0 = 0)$ as a function of λ_0 for different Fermi energies.

Finally, we would like to address the issue of laser-induced optical current. The result for the conductivity of a dissipative optical current can be obtained from the calculated complex polarization function $\Pi_0(q, \omega | \phi, \lambda_0)$. Specifically, the optical-current conductivity in the long-wavelength limit is given by $\sigma_O(\omega | \phi, \lambda_0) = \lim_{q \rightarrow 0} \{ (ie^2 \omega / q^2) \Pi_0(q, \omega | \phi, \lambda_0) \}$.²³ Consequently, the real part of $\sigma_O(\omega | \phi, \lambda_0)$ for optical current will correspond to the imaginary part of $\Pi_0(q, \omega | \phi, \lambda_0)$ for absorptive dissipation. On the other hand, the imaginary part of $\sigma_O(\omega | \phi, \lambda_0)$ will be associated with the real part of $\Pi_0(q, \omega | \phi, \lambda_0)$ for induced polarization.

Our numerical results for calculated optical-current conductivity in a dice lattice are presented in Fig. 4. Its real part $\text{Re}[\sigma_O(\omega | \lambda_0)]$ presented in Fig. 4(a) reveals that a high plateau starting nearly from $\hbar\omega = E_F$ extends well into a high-frequency region, and it is slightly enhanced by laser irradiation from the result $\simeq 1 + 4\lambda_0^4$ for graphene.^{57,58} This is in correspondence with an appearance of Landau damping for plasmon modes in the $q \rightarrow 0$ limit, as displayed in Fig. 3(c). In addition, for the imaginary part $\text{Im}[\sigma_O(\omega | \lambda_0)]$, we find it independent of λ_0 except for $\hbar\omega$ close to E_F . Furthermore, a negative peak in $\text{Im}[\sigma_O(\omega | \lambda_0)]$ shows up at $\hbar\omega = E_F$ and becomes sharpened by increasing λ_0 due to laser irradiation. Moreover, $\text{Im}[\sigma_O(\omega | \lambda_0)]$ in the region of $\hbar\omega > 2E_F$ is fully suppressed to zero in the long-wavelength limit $q \rightarrow 0$. This is related to the fact that plasmon modes, determined by $\text{Re}[\Pi_0(q, \omega | \lambda_0)] = q/2\pi\alpha_0$, do not exist in this region as $q \rightarrow 0$, as can be verified from Fig. 3(d).

IV. IMPURITY SCATTERING AND CONDUCTION CURRENT

Now, we consider the transport conductivity $\sigma_T(\lambda_0)$ of an irradiated dice lattice. We will calculate $\sigma_T(\lambda_0)$ in the relaxation-time approximation, while the scattering potential is assumed as the point-like Coulomb interaction $U_{im}(r) = Z^* e / (4\pi\epsilon_0\epsilon_r r)$ with an impurity charge number Z^* . For finite electron doping $E_F > 0$, the inverse relaxation time is given by^{59–62}

$$\frac{1}{\tau(k, \lambda_0)} = \frac{n_i}{2\pi\hbar} \int_0^{2\pi} d\beta_{\mathbf{k}, \mathbf{k}'} (1 - \cos \beta_{\mathbf{k}, \mathbf{k}'}) \times \sum_{\tau=\pm 1} \int_0^\infty \frac{k' dk'}{|\epsilon(|\mathbf{k} - \mathbf{k}'|, \omega = 0)|^2} \left| \int d^2\mathbf{r} \Phi_\gamma^\tau(\mathbf{r}, \mathbf{k}', \lambda_0) U_{im}(r) \Phi_\gamma^\tau(\mathbf{r}, \mathbf{k}, \lambda_0) \right|^2 \delta[\epsilon_\gamma(k, \lambda_0) - \epsilon_\gamma(k', \lambda_0)], \quad (4)$$

where $\gamma = +$, n_i represents the impurity areal density, $\beta_{\mathbf{k}, \mathbf{k}'}$ is the angle between electron wavevectors \mathbf{k} and \mathbf{k}' , the full electron wave function is $\Phi_\gamma^\tau(\mathbf{r}, \mathbf{k}, \lambda_0) = \Psi_\gamma^\tau(\mathbf{k}, \lambda_0) \exp(i\mathbf{k} \cdot \mathbf{r})$. For isotropic band dispersions and electronic states, corresponding to circularly-polarized laser irradiation, the relaxation time, $\tau(k, \lambda_0)$, depends only on $k = |\mathbf{k}|$. In the absence of static screening, $\tau(k, \lambda_0)$ could be obtained analytically (see Appendix C).

For the isotropic case of circularly-polarized irradiation and at low temperatures, the electric-current J_0 per length under an applied DC electric field E_0 is expressed as (see Appendix C)

$$J_0 = \left(\frac{e}{\pi}\right)^2 E_0 \int d^2\mathbf{k} [v_\gamma(k, \lambda_0)]^2 \tau(k, \lambda_0) \delta[\epsilon_\gamma(k, \lambda_0) - E_F], \quad (5)$$

where $v_\gamma(k, \lambda_0) = (1/\hbar) \partial \varepsilon_\gamma(k, \lambda_0) / \partial k$ is the electron group velocity.

The inverse relaxation time $1/\tau_0(k)$ for a non-irradiated dice lattice is 3/4 times of that of graphene due to the change of wave-function overlap factors, which for graphene is equal to $(1 + \cos \beta_{\mathbf{k}, \mathbf{k}'})^2/4$. Dice lattice and graphene represent two limiting cases of $\alpha - \mathcal{T}_3$ lattices, and their $\tau_0(k)$ has already been calculated.⁵⁶ Once the circularly-polarized laser is applied, the ratio of inverse relaxation times becomes $\tau_0(k)/\tau(k, \lambda_0) \simeq 3\pi/4 - 7\pi/16 \xi^2 + \dots$, where $\xi = c_0 \lambda_0 / E_F = (e \mathcal{E}_0 / \hbar \omega)^2 (v_F / \omega k_F)$. This apparently leads to a substantial drop of $\sigma_T(\lambda_0)$ in the presence of a laser field \mathcal{E}_0 . The exact ratio is predetermined by a pseudospin-1 wave function with three inequivalent components, and is not valid for graphene or a 2D electron gas.

Another factor for laser-induced reduction of $\sigma_T(\lambda_0)$ comes from the decreased electron group velocity $v_\gamma(k, \lambda_0)$. From Eq. (1), we find $[v_F(\lambda_0)]^2 \simeq v_F^2 (1 - \lambda_0^2/4)^2 [1 - (\lambda_0^2/4)(c_0/E_F)^2]$. Here, the two terms are related to the variation of the Fermi velocity v_F and the opening of a bandgap $E_G = \lambda_0 c_0$, respectively. Both of these effects lead to a decrease in $\sigma_T(\lambda_0)$ with λ_0 . Using $\mathbb{I}_0 = 10 \text{ W/cm}^2$ and $c_0/E_F \simeq 9.75$, we find the magnitude of the second term is much larger than the first term. Besides, the screening factor is also reduced in the presence of a laser field which must be taken into account for an accurate determination of $\sigma_T(\lambda_0)$.

The above obtained results for a dice lattice are quite different from those of graphene. For graphene, we get $[v_F(\lambda_0)]^2/v_F^2 \simeq 1 - \lambda_0^2 (c_0/E_F)^2$, and then, the inverse relaxation time $\tau_0/\tau(k, \lambda_0) \simeq 1 - 3\lambda_0^2 (c_0/E_F)^2$,⁴⁵ as well as the reduced transport conductivity $\sigma_T(\lambda_0)/\sigma_T(\lambda_0 = 0) \simeq 1 - 4\lambda_0^2 (c_0/E_F)^2$.

Numerical results for the relaxation-time $\tau(k, \lambda_0)/\tau_0$ and the transport-conductivity $\sigma_T(\lambda_0)/\sigma_T(\lambda_0 = 0)$ in a dice lattice are presented in Fig. 5, including the laser-induced modification to the static screening for elastic scattering between electrons and impurities. From Fig. 5(a), we find the relaxation time $\tau(k, \lambda_0)$ is approximately proportional to k and decreases with increasing λ_0 . Moreover, the laser-induced modification (dashed curves) to the static dielectric function is important quantitatively. From Fig. 5(b), we know the transport conductivity $\sigma_T(\lambda_0)$ decreases with λ_0 nonlinearly compared to the result in the absence of a laser field, which agrees with our analytical evaluations. In addition, for fixed λ_0 this reduction effect becomes less and less significant with increasing Fermi energy since the correction is proportional to c_0/E_F .

V. CONCLUDING REMARKS AND SUMMARY

In this paper, we have calculated and analyzed numerical results for plasmon-mode dispersion and damping as well as their effects on displacement and transport currents of electrons in irradiated $\alpha - \mathcal{T}_3$ materials by a circularly-polarized laser. As a result, we conclude that the intensity of a laser field can be used effectively to control both optical and transport conductivities in the system, in addition to a tuning of them with a structure parameter $0 < \alpha \leq 1$ for different $\alpha - \mathcal{T}_3$ lattices.

In particular, for the whole range of α values, we observe that the tuning of plasmon modes reaches the strongest as $\phi \simeq 0$ on the graphene side, but it becomes relatively weak as $\phi \simeq \pi/4$ on the dice-lattice side. Meanwhile, a significant increase in the plasmon damping above the Fermi level, accompanied by a change of plasmon dispersion below the Fermi energy, is found with increasing α from zero to one. Moreover, the pinching of plasmon dispersion around the Fermi energy also shows up, which can be attributed to electron transitions from the middle flat band to the upper Dirac cone.

After a circularly-polarized laser has been applied to a dice lattice, the plasmon mode is modified dramatically by lowering its dispersion curve below the main diagonal. Meanwhile, the transport conductivity of electrons in a dice lattice decreases with increasing laser intensity. These results indicate that electron dynamics under irradiation in graphene is quite different from that in a dice lattice and can be controlled by laser, which further implies that such a difference can be tuned by a structure parameter α for $\alpha - \mathcal{T}_3$ materials. All of these are expected to provide very useful information and guidance for designing nano-electronic and nano-plasmonic devices based on innovative low-dimensional $\alpha - \mathcal{T}_3$ materials.

Acknowledgments

D.H. would thank the support from the Air Force Office of Scientific Research (AFOSR). D.H is also supported by the DoD Lab-University Collaborative Initiative (LUCI) program. G.G. would like to acknowledge the support from the Air Force Research Laboratory (AFRL) through Grant #12530960.

Appendix A: Laser-Renormalized Electronic States

The low-energy Hamiltonian for a dice lattice irradiated by a laser field under the off-resonance condition can be obtained from a perturbation theory by using the Floquet-Magnus expansion⁴⁸, given by

$$\mathbb{H}_\tau(k|\theta_{\mathbf{k}}) = -\tau\lambda_0 \frac{c_0}{2} \hat{\Sigma}_z + \frac{\hbar}{\sqrt{2}} \mathcal{V}_F(\lambda_0) \sum_{s=\pm} \hat{\Sigma}_s k_\tau^s, \quad (\text{A1})$$

where $c_0 = e\mathcal{E}_0 v_F/\omega$ is the interaction energy, $\lambda_0 = c_0/(\hbar\omega)$ is a small dimensionless light-electron coupling constant used for the expansion, $\mathcal{V}_F(\lambda_0) = [1 - (\lambda_0/2)^2] v_F$ is the renormalized Fermi velocity, $k_\tau^\pm = \tau k_x \pm i k_y = \tau k e^{i\tau\theta_{\mathbf{k}}}$, and $\theta_{\mathbf{k}} = \tan^{-1}(k_y/k_x)$. Additionally, $\hat{\Sigma}_\pm = \hat{\Sigma}_x \pm i\hat{\Sigma}_y$, where $\hat{\Sigma}_{x,y,z}$ are three-dimensional Pauli matrices defined in Ref. [48].

Energy dispersions of the electron dressed states associated with the Hamiltonian in Eq. (A1) are found for $\gamma = \pm$ to be

$$\begin{aligned} \varepsilon_0(k, \lambda_0) &= 0 \quad \text{and} \\ \varepsilon_\gamma(k, \lambda_0) &= \gamma \left\{ (\hbar v_F k)^2 \left[1 - \left(\frac{\lambda_0}{2} \right)^2 \right]^2 + c_0^2 \left(\frac{\lambda_0}{2} \right)^2 \right\}^{1/2}. \end{aligned} \quad (\text{A2})$$

This gives rise to an energy bandgap $E_G = \lambda_0 c_0 \equiv 2\Delta_0$ which is exactly one half the graphene bandgap under the same irradiation, while renormalized Fermi velocity stays the same as that of graphene. Clearly, the obtained dispersions do not depend on the valley index $\tau = \pm 1$.

Furthermore, the electron wave functions for an irradiated dice lattice are calculated as

$$\Psi_\gamma^\tau(\mathbf{k}, \lambda_0) = \frac{1}{\sqrt{\mathcal{N}_\gamma^\tau}} \begin{bmatrix} \tau \mathcal{C}_{1,\gamma}^\tau e^{-i\tau\theta_{\mathbf{k}}} \\ \mathcal{C}_{2,\gamma}^\tau \\ \tau (\hbar v_F k)^2 e^{+i\tau\theta_{\mathbf{k}}} \end{bmatrix}, \quad (\text{A3})$$

where

$$\begin{aligned} \mathcal{C}_{1,\gamma}^\tau(k, \lambda_0) &= (\hbar v_F k)^2 + 2 \left(\delta_\lambda^2 - \gamma\tau\delta_\lambda \sqrt{(\hbar v_F k)^2 + \delta_\lambda^2} \right), \\ \mathcal{C}_{2,\gamma}^\tau(k, \lambda_0) &= \sqrt{2}\gamma (\hbar v_F k) \left(\sqrt{(\hbar v_F k)^2 + \delta_\lambda^2} - \gamma\tau\delta_\lambda \right), \\ \mathcal{N}_\gamma^\tau(k, \lambda_0 \ll 1) &\simeq 4(\hbar v_F k)^4 - 4\gamma\tau c_0 \lambda_0 (\hbar v_F k)^3 + 3[c_0 \lambda_0 (\hbar v_F k)]^2 + \dots \end{aligned} \quad (\text{A4})$$

Here, our parameter $\delta_\lambda = 2\lambda_0 c_0/(4 - \lambda_0^2)$ is different from the energy gap $E_G = \lambda_0 c_0 = 2\Delta_0$. For $\gamma = +1$, the wave function in Eq. (A3) for the conduction band, can be simply rewritten as

$$\Psi_\gamma^\tau(\mathbf{k}, \lambda_0) = \begin{bmatrix} \tau c_1^{(+1)} e^{-i\tau\theta_{\mathbf{k}}} \\ c_2^{(+1)} \\ \tau c_3^{(+1)} e^{+i\tau\theta_{\mathbf{k}}} \end{bmatrix}, \quad (\text{A5})$$

where

$$\begin{aligned} c_1^{(+1)} &= \frac{\mathcal{C}_{1,\gamma=1}^\tau}{\sqrt{\mathcal{N}_{\gamma=1}^\tau}}, & \left(c_1^{(+1)} \right)^2 &\simeq \frac{1}{4} - \frac{\lambda_0}{4} \frac{c_0}{\hbar v_F k} \tau + \frac{\lambda_0^2}{16} \left(\frac{c_0}{\hbar v_F k} \right)^2 \dots, \\ c_2^{(+1)} &= \frac{\mathcal{C}_{2,\gamma=1}^\tau}{\sqrt{\mathcal{N}_{\gamma=1}^\tau}}, & \left(c_2^{(+1)} \right)^2 &\simeq \frac{1}{2} - \frac{\lambda_0^2}{8} \left(\frac{c_0}{\hbar v_F k} \right)^2 + \dots, \\ c_3^{(+1)} &= \frac{(\hbar v_F k)^2}{\sqrt{\mathcal{N}_{\gamma=1}^\tau}}, & \left(c_3^{(+1)} \right)^2 &\simeq \frac{1}{4} + \frac{\lambda_0}{4} \frac{c_0}{\hbar v_F k} \tau + \frac{\lambda_0^2}{16} \left(\frac{c_0}{\hbar v_F k} \right)^2 + \dots \end{aligned} \quad (\text{A6})$$

For the flat band, on the other hand, we obtain

$$\Psi_0^\tau(\mathbf{k}, \lambda_0) = \frac{1}{\sqrt{\mathcal{N}_{\gamma=0}^\tau}} \begin{bmatrix} \hbar v_F k e^{-i\tau\theta_{\mathbf{k}}} \\ 2\sqrt{2} c_0 \lambda_0 / (4 - \lambda_0^2) \\ -\hbar v_F k e^{+i\tau\theta_{\mathbf{k}}} \end{bmatrix}, \quad (\text{A7})$$

where

$$\mathcal{N}_{\gamma=0}^\tau(k, \lambda_0 \ll 1) \simeq 2(\hbar v_F k)^2 + \frac{1}{2} (\lambda_0 c_0)^2 + \dots \quad (\text{A8})$$

Here, the wave-function components are no longer equal to each other, as expected for a finite energy gap.

The obtained wave function (A7) could be rewritten as

$$\Psi_0^\tau(\mathbf{k}, \lambda_0) = \begin{bmatrix} c_1^{(0)} e^{-i\tau\theta_{\mathbf{k}}} \\ c_2^{(0)} \\ -c_1^{(0)} e^{+i\tau\theta_{\mathbf{k}}} \end{bmatrix}, \quad (\text{A9})$$

where

$$\begin{aligned} c_1^{(0)} &= \frac{\hbar v_F k}{\sqrt{\mathcal{N}_0}}, & (c_1^{(0)})^2 &\simeq \frac{1}{2} - \frac{1}{8} \left(\frac{\lambda_0 c_0}{\hbar v_F k} \right)^2 + \dots, \\ c_2^{(0)} &= \frac{2\sqrt{2}\lambda_0}{4 - \lambda_0^2} \frac{c_0}{\sqrt{\mathcal{N}_0}}, & (c_2^{(0)})^2 &\simeq \frac{1}{4} \left(\frac{\lambda_0 c_0}{\hbar v_F k} \right)^2 + \dots \end{aligned} \quad (\text{A10})$$

Here, it is important to notice that the laser-induced corrections to the flat band wave function do not depend on the valley index τ in contrast to the cases with $\gamma = \pm 1$.

Appendix B: Wave-Function Overlap

The prefactor, or the overlap of two electronic states, is defined by a scalar product $\mathbb{O}_{\gamma, \gamma'}^\tau(\mathbf{k}, \mathbf{k}' | \phi, \lambda_0)$ of the initial $\Psi_\gamma^\tau(\mathbf{k}, \lambda_0)$ and scattered $\Psi_{\gamma'}^\tau(\mathbf{k}', \lambda_0)$ electronic states with the wave vectors \mathbf{k} and $\mathbf{k}' = \mathbf{k} + \mathbf{q}$

$$\begin{aligned} \mathbb{O}_{\gamma, \gamma'}^\tau(\mathbf{k}, \mathbf{k} + \mathbf{q} | \phi, \lambda_0) &= \left| \mathbb{S}_{\gamma, \gamma'}^\tau(\mathbf{k}, \mathbf{k} + \mathbf{q} | \phi, \lambda_0) \right|^2, \\ \mathbb{S}_{\gamma, \gamma'}^\tau(\mathbf{k}, \mathbf{k} + \mathbf{q} | \phi, \lambda_0) &= \left\langle \Psi_\gamma^\tau(\mathbf{k}, \lambda_0) \left| \Psi_{\gamma'}^\tau(\mathbf{k} + \mathbf{q}, \lambda_0) \right. \right\rangle, \end{aligned} \quad (\text{B1})$$

where $k' = \sqrt{k^2 + q^2 + 2kq \cos \beta_{\mathbf{k}, \mathbf{k}'}}$ and $\beta_{\mathbf{k}, \mathbf{k}'} = \theta_{\mathbf{k}'} - \theta_{\mathbf{k}}$.

For an irradiated ($\lambda_0 > 0$) dice lattice with $\phi = \pi/4$ and $\tau = +1$, we obtain

$$\mathbb{S}_{0, +1}(\mathbf{k}, \mathbf{k}' | \phi = \pi/4, \lambda_0) = c_1^{(0)}(k) c_1^{(+1)}(k') e^{-i\tau\beta_{\mathbf{k}, \mathbf{k}'}} + c_2^{(0)}(k) c_2^{(+1)}(k') - c_1^{(0)}(k) c_3^{(+1)}(k') e^{+i\tau\beta_{\mathbf{k}, \mathbf{k}'}} , \quad (\text{B2})$$

which corresponds to the transitions from the flat band $\gamma = 0$ to the conduction band with $\gamma' = +1$, ($0 \leftrightarrow +1$ and back. Similarly, we have

$$\mathbb{S}_{-1, +1}(\mathbf{k}, \mathbf{k}' | \phi = \pi/4, \lambda_0) = c_1^{(-1)}(k) c_1^{(+1)}(k') e^{-i\tau\beta_{\mathbf{k}, \mathbf{k}'}} + c_2^{(-1)}(k) c_2^{(+1)}(k') + c_3^{(-1)}(k) c_3^{(+1)}(k') e^{+i\tau\beta_{\mathbf{k}, \mathbf{k}'}} \quad (\text{B3})$$

for the transitions between the valence $\gamma = -1$ and conduction band with $\gamma' = +1$, ($-1 \leftrightarrow +1$), and finally,

$$\mathbb{S}_{+1, +1}(\mathbf{k}, \mathbf{k}' | \phi = \pi/4, \lambda_0) = c_1^{(+1)}(k) c_1^{(+1)}(k') e^{-i\tau\beta_{\mathbf{k}, \mathbf{k}'}} + c_2^{(+1)}(k) c_2^{(+1)}(k') + c_3^{(+1)}(k) c_3^{(+1)}(k') e^{+i\tau\beta_{\mathbf{k}, \mathbf{k}'}} . \quad (\text{B4})$$

We exclude the remaining possible transitions $-1 \leftrightarrow -1$ inside the valence band and between the flat and valences bands $0 \leftrightarrow -1$, which are inactive at zero temperature for electron doping ($E_F > 0$). In the absence of irradiation ($\lambda_0 = 0$), these three overlap factors are given in Table C.

Appendix C: Laser-Renormalized Electron Transport

For a finite electron doping $E_F > 0$, the inverse relaxation time is calculated as

$$\begin{aligned} \frac{1}{\tau(k, \lambda_0)} &= \frac{n_i}{2\pi\hbar} \int_0^{2\pi} d\beta_{\mathbf{k}, \mathbf{k}'} (1 - \cos \beta_{\mathbf{k}, \mathbf{k}'}) \\ &\times \sum_{\tau=\pm 1} \int_0^\infty \frac{k' dk'}{|\epsilon(\mathbf{k} - \mathbf{k}', \omega = 0)|^2} \left| \int d^2\mathbf{r} \Phi_\gamma^\tau(\mathbf{r}, \mathbf{k}', \lambda_0) U_{im}(r) \Phi_\gamma^\tau(\mathbf{r}, \mathbf{k}, \lambda_0) \right|^2 \delta[\varepsilon_\gamma(k, \lambda_0) - \varepsilon_\gamma(k', \lambda_0)] , \end{aligned} \quad (\text{C1})$$

where $\beta_{\mathbf{k}, \mathbf{k}'}$ is the angle between \mathbf{k} and \mathbf{k}' , the complete wave function is $\Phi_\gamma^\tau(\mathbf{r}, \mathbf{k}, \lambda_0) = \Psi_\gamma^\tau(\mathbf{r}, \mathbf{k}, \lambda_0) \exp(i\mathbf{k} \cdot \mathbf{r})$, and $\gamma = +1$. For isotropic dispersions and electronic states, corresponding to the circularly-polarized irradiation, the relaxation time depends only on $k = |\mathbf{k}|$.

In our analytical evaluation, we neglect the static-screening factor $1/|\epsilon(q, \omega = 0)|^2$ in Eq. (C1). Since we concentrate on the ratio of two inverse relaxation times with/without irradiation, we expect only the change in static dielectric function with λ_0 will be ignored. We begin with the scattering potential matrix element in Eq. (C1), given by

$$\mathbb{W}_\gamma^\tau(\mathbf{k}, \mathbf{k}') = \int d^2\mathbf{r} \Phi_\gamma^\tau(\mathbf{r}, \mathbf{k}', \lambda_0) U_{im}(r) \Phi_\gamma^\tau(\mathbf{r}, \mathbf{k}, \lambda_0) , \quad (\text{C2})$$

where $U_{im}(r) = e^2/(4\pi\epsilon_0\epsilon_r r) \equiv \alpha_0/r$. As a result, we get

$$\mathbb{W}_\gamma^\tau(\mathbf{k}, \mathbf{k}') = \alpha_0 \mathbb{S}_{\gamma, \gamma}^\tau(\mathbf{k}, \mathbf{k}' | \phi, \lambda_0) \int \frac{d^2\mathbf{r}}{r} \exp[i(\mathbf{k} - \mathbf{k}') \cdot \mathbf{r}] \equiv U_0(|\mathbf{k} - \mathbf{k}'|) \mathbb{S}_{\gamma, \gamma}^\tau(\mathbf{k}, \mathbf{k}' | \phi, \lambda_0) , \quad (\text{C3})$$

where $\mathbb{S}_{\gamma, \gamma}^\tau(\mathbf{k}, \mathbf{k}' | \phi, \lambda_0)$ is defined in Eq. (B1) and

$$U_0(q) = \alpha_0 \int d^2\mathbf{r} \frac{\exp(i\mathbf{q} \cdot \mathbf{r})}{r} = \frac{2\pi\alpha_0}{q} . \quad (\text{C4})$$

The transition rate in the Born approximation is written as

$$\mathbb{T}_\gamma^\tau(\mathbf{k}, \mathbf{k}') = \frac{2\pi}{\hbar} \left| \mathbb{W}_\gamma^\tau(\mathbf{k}, \mathbf{k}') \right|^2 \delta[\varepsilon_\gamma(k, \lambda_0) - \varepsilon_\gamma(k', \lambda_0)] , \quad (\text{C5})$$

where

$$\begin{aligned} \delta[\varepsilon_\gamma(k, \lambda_0) - \varepsilon_\gamma(k', \lambda_0)] &= \frac{\delta(k - k')}{\hbar v_F} , \\ |\mathbf{k} - \mathbf{k}'| &= 2k \sin\left(\frac{\beta_{\mathbf{k}, \mathbf{k}'}}{2}\right) . \end{aligned} \quad (\text{C6})$$

By using the result in Eq. (C5), the inverse relaxation time can be formally written as

$$\frac{1}{\tau_\gamma(k, \lambda_0)} = \sum_{\tau=\pm 1} \frac{n_i}{(2\pi)^2} \int_0^{2\pi} d\beta_{\mathbf{k}, \mathbf{k}'} (1 - \cos \beta_{\mathbf{k}, \mathbf{k}'}) \int_0^\infty k' dk' \mathbb{T}_\gamma^\tau(\mathbf{k}, \mathbf{k}') \Big|_{k'=k} . \quad (\text{C7})$$

Specifically, for $\gamma = +1$ we find

$$\begin{aligned} \frac{1}{\tau(k, \lambda_0)} &= \frac{\pi n_i}{2v_F} \left(\frac{\alpha_0}{\hbar}\right)^2 \frac{1}{k} \mathbb{I}(k, \lambda_0) , \\ \mathbb{I}(k, \lambda_0) &= \int_0^{2\pi} d\beta_{\mathbf{k}, \mathbf{k}'} \left(\left\{ \left[\left(c_1^{(+1)}(k, \lambda_0) \right)^2 + \left(c_3^{(+1)}(k, \lambda_0) \right)^2 \right] \cos \beta_{\mathbf{k}, \mathbf{k}'} + \left(c_2^{(+1)}(k, \lambda_0) \right)^2 \right\}^2 \right. \\ &\quad \left. + \left\{ \left[\left(c_1^{(+1)}(k, \lambda_0) \right)^2 - \left(c_3^{(+1)}(k, \lambda_0) \right)^2 \right] \sin \beta_{\mathbf{k}, \mathbf{k}'} \right\}^2 \right) . \end{aligned} \quad (\text{C8})$$

Material	Overlap	Inverse relaxation time
Graphene	$(1 + \cos \beta_{\mathbf{k}, \mathbf{k}'})/2$	π
Dice lattice	$(1 + \cos \beta_{\mathbf{k}, \mathbf{k}'})^2/4$	$3\pi/4$
$\alpha - \overline{\mathcal{T}}_3$	$(1/4) [(1 + \cos \beta_{\mathbf{k}, \mathbf{k}'})^2 + \cos^2(2\phi) \sin^2 \beta_{\mathbf{k}, \mathbf{k}'}]$	$(\pi/8) [7 + \cos(4\phi)]$

TABLE I: Prefactors (wave-function overlaps), and inverse relaxation time $\mathbb{I}(k)$ factor from Eq. (C8) for graphene and general $\alpha - \overline{\mathcal{T}}_3$ materials in the absence of external irradiation ($\lambda_0 = 0$).

Finally, by using the relaxation-time approximation, the electric current \mathbf{J}_0 per length is calculated as

$$\mathbf{J}_0 = \left(\frac{e}{\pi}\right)^2 \int d^2\mathbf{k} \tau(k, \lambda_0) \mathbf{v}(\mathbf{k}) [\mathbf{E}_0 \cdot \mathbf{v}(\mathbf{k})] \left[-\frac{\partial f_0[\varepsilon(k, \lambda_0) - \mu_0]}{\partial \varepsilon(k, \lambda_0)} \right], \quad (\text{C9})$$

where \mathbf{E}_0 represents the external DC electric field, $\mathbf{v}(\mathbf{k}) = (1/\hbar) \partial \varepsilon(k, \lambda_0) / \partial \mathbf{k}$ is the group velocity of electrons, $f_0[\varepsilon(k, \lambda_0) - \mu_0] = \{1 + \exp[(\varepsilon(k, \lambda_0) - \mu_0)/k_B T]\}^{-1}$ is the thermal-equilibrium distribution function for electrons, μ_0 is the chemical potential, and T is the system temperature. If $T = 0$ K, we simply have $\partial f_0[\varepsilon(k, \lambda_0) - \mu_0] / \partial \varepsilon(k, \lambda_0) = \delta[\varepsilon(k, \lambda_0) - E_F]$ with Fermi energy E_F and the integral in Eq. (C9) can be performed analytically.

-
- ¹ A. Raoux, M. Morigi, J.-N. Fuchs, F. Piéchon, and G. Montambaux, Physical review letters **112**, 026402 (2014).
 - ² J. Vidal, R. Mosseri, and B. Douçot, Physical review letters **81**, 5888 (1998).
 - ³ M. Vigh, L. Oroszlány, S. Vajna, P. San-Jose, G. Dávid, J. Cserti, and B. Dóra, Physical Review B **88**, 161413 (2013).
 - ⁴ M. Rizzi, V. Cataudella, and R. Fazio, Physical Review B **73**, 144511 (2006).
 - ⁵ K. Novoselov, A. K. Geim, S. Morozov, D. Jiang, M. Katsnelson, I. Grigorieva, S. Dubonos, and A. Firsov, nature **438**, 197 (2005).
 - ⁶ D. Leykam, A. Andreanov, and S. Flach, Advances in Physics: X **3**, 1473052 (2018).
 - ⁷ J. D. Malcolm and E. J. Nicol, Physical Review B **93**, 165433 (2016).
 - ⁸ J. Romhányi, K. Penc, and R. Ganesh, Nature communications **6**, 6805 (2015).
 - ⁹ X. Huang, Y. Lai, Z. H. Hang, H. Zheng, and C. Chan, Nature materials **10**, 582 (2011).
 - ¹⁰ Y. Li, S. Kita, P. Muñoz, O. Reshef, D. I. Vulis, M. Yin, M. Lončar, and E. Mazur, Nature Photonics **9**, 738 (2015).
 - ¹¹ R. A. Vicencio, C. Cantillano, L. Morales-Inostroza, B. Real, C. Mejía-Cortés, S. Weimann, A. Szameit, and M. I. Molina, Physical review letters **114**, 245503 (2015).
 - ¹² S. Mukherjee, A. Spracklen, D. Choudhury, N. Goldman, P. Öhberg, E. Andersson, and R. R. Thomson, Physical review letters **114**, 245504 (2015).
 - ¹³ E. Illes, Ph.D. thesis (2017).
 - ¹⁴ E. Illes and E. Nicol, Physical Review B **94**, 125435 (2016).
 - ¹⁵ E. Illes, J. P. Carbotte, and E. J. Nicol, Phys. Rev. B **92**, 245410 (2015).
 - ¹⁶ B. Dey and T. K. Ghosh, Physical Review B **98**, 075422 (2018).
 - ¹⁷ B. Dey and T. K. Ghosh, Physical Review B **99**, 205429 (2019).
 - ¹⁸ T. Biswas and T. K. Ghosh, Journal of Physics: Condensed Matter **30**, 075301 (2018).
 - ¹⁹ T. Biswas and T. K. Ghosh, Journal of Physics: Condensed Matter **28**, 495302 (2016).
 - ²⁰ S. F. Islam and P. Dutta, Phys. Rev. B **96**, 045418 (2017).
 - ²¹ A. D. Kovács, G. Dávid, B. Dóra, and J. Cserti, Phys. Rev. B **95**, 035414 (2017).
 - ²² F. Piéchon, J. Fuchs, A. Raoux, and G. Montambaux, in *Journal of Physics: Conference Series* (IOP Publishing, 2015), vol. 603, p. 012001.
 - ²³ C. J. Tabert and E. J. Nicol, Physical Review B **89**, 195410 (2014).
 - ²⁴ M. Katsnelson, K. Novoselov, and A. Geim, Nature physics **2**, 620 (2006).
 - ²⁵ E. Illes and E. Nicol, Physical Review B **95**, 235432 (2017).
 - ²⁶ G. Gumbs, A. Iurov, D. Huang, and L. Zhemchuzhna, Physical Review B **89**, 241407 (2014).
 - ²⁷ E. Gorbar, V. Gusynin, and D. Oriekhov, Physical Review B **99**, 155124 (2019).
 - ²⁸ P. Perez-Piskunow, G. Usaj, C. Balseiro, and L. F. Torres, Physical Review B **89**, 121401 (2014).
 - ²⁹ H. L. Calvo, H. M. Pastawski, S. Roche, and L. E. F. Torres, Applied Physics Letters **98**, 232103 (2011).
 - ³⁰ E. S. Morell and L. E. F. Torres, Physical Review B **86**, 125449 (2012).
 - ³¹ Z. Gu, H. Fertig, D. P. Arovas, and A. Auerbach, Physical review letters **107**, 216601 (2011).
 - ³² V. Dal Lago, E. S. Morell, and L. F. Torres, Physical Review B **96**, 235409 (2017).
 - ³³ G. Usaj, P. Perez-Piskunow, L. F. Torres, and C. Balseiro, Physical Review B **90**, 115423 (2014).
 - ³⁴ I. Iorsh, K. Dini, O. Kibis, and I. Shelykh, Physical Review B **96**, 155432 (2017).
 - ³⁵ N. Goldman and J. Dalibard, Physical review X **4**, 031027 (2014).

- ³⁶ O. Kibis, *Physical Review B* **81**, 165433 (2010).
- ³⁷ A. Iurov, G. Gumbs, O. Roslyak, and D. Huang, *Journal of Physics: Condensed Matter* **24**, 015303 (2011).
- ³⁸ O. Kibis, K. Dini, I. Iorsh, and I. Shelykh, *Physical Review B* **95**, 125401 (2017).
- ³⁹ O. Kibis, K. Dini, I. Iorsh, and I. Shelykh, *Semiconductors* **52**, 523 (2018).
- ⁴⁰ O. Kyriienko, O. Kibis, and I. Shelykh, *Physical Review B* **99**, 115411 (2019).
- ⁴¹ A. Iurov, G. Gumbs, D. Huang, and L. Zhemchuzhna, *Journal of Applied Physics* **121**, 084306 (2017).
- ⁴² A. Iurov, G. Gumbs, and D. Huang, *Journal of Modern Optics* **64**, 913 (2017).
- ⁴³ S. Morina, K. Dini, I. V. Iorsh, and I. A. Shelykh, *ACS Photonics* **5**, 1171 (2018).
- ⁴⁴ S. Morina, O. V. Kibis, A. A. Pervishko, and I. A. Shelykh, *Phys. Rev. B* **91**, 155312 (2015).
- ⁴⁵ K. Kristinsson, O. Kibis, S. Morina, and I. Shelykh, *Scientific reports* **6**, 20082 (2016).
- ⁴⁶ P. Pyatkovskiy, *Journal of Physics: Condensed Matter* **21**, 025506 (2008).
- ⁴⁷ A. Iurov, L. Zhemchuzhna, G. Gumbs, and D. Huang, *Journal of Applied Physics* **122**, 124301 (2017).
- ⁴⁸ A. Iurov, G. Gumbs, and D. Huang, *Physical Review B* **99**, 205135 (2019).
- ⁴⁹ V. Kozin, I. Iorsh, O. Kibis, and I. Shelykh, *Physical Review B* **97**, 035416 (2018).
- ⁵⁰ A. Politano and G. Chiarello, *Nanoscale* **6**, 10927 (2014).
- ⁵¹ B. Wunsch, T. Stauber, F. Sols, and F. Guinea, *New Journal of Physics* **8**, 318 (2006).
- ⁵² A. Scholz, T. Stauber, and J. Schliemann, *Physical Review B* **88**, 035135 (2013).
- ⁵³ G. Gumbs, A. Balassis, A. Iurov, and P. Fekete, *The Scientific World Journal* **2014** (2014).
- ⁵⁴ J. Tempere, I. F. Silvera, and J. T. Devreese, *Phys. Rev. B* **65**, 195418 (2002).
- ⁵⁵ A. Iurov, G. Gumbs, B. Gao, and D. Huang, *Applied Physics Letters* **104**, 203103 (2014).
- ⁵⁶ D. Huang, A. Iurov, H.-Y. Xu, Y.-C. Lai, and G. Gumbs, *Physical Review B* **99**, 245412 (2019).
- ⁵⁷ A. Iurov, G. Gumbs, and D. Huang, *Physical Review B* **98**, 075414 (2018).
- ⁵⁸ L. A. Falkovsky and S. S. Pershoguba, *Phys. Rev. B* **76**, 153410 (2007).
- ⁵⁹ T. Ando, A. B. Fowler, and F. Stern, *Reviews of Modern Physics* **54**, 437 (1982).
- ⁶⁰ E. Hwang and S. D. Sarma, *Physical Review B* **79**, 165404 (2009).
- ⁶¹ A. C. Neto, F. Guinea, N. M. Peres, K. S. Novoselov, and A. K. Geim, *Reviews of modern physics* **81**, 109 (2009).
- ⁶² E. H. Hwang and S. Das Sarma, *Phys. Rev. B* **77**, 195412 (2008).